Proceedings of DETC2002
2002 ASME Design Engineering Technical Conferences
September 29-October 2, 2002, Montreal, Canada

DETC2002/MECH-34221

WHEELED OMNI-DIRECTIONAL ROBOT DYNAMICS INCLUDING SLIP

Robert L. Williams II and **Brian E. Carter**
Ohio University
Athens, OH

Paolo Gallina and **Giulio Rosati**
University of Padova
Italy

ABSTRACT

A dynamic model is presented for omni-directional wheeled mobile robots, including wheel/motion surface slip. We derive the dynamics model, experimentally measure friction coefficients, and measure the force to cause slip (to validate our friction model). Dynamic simulation examples are then presented to demonstrate omni-directional motion with slip. After developing an improved friction model, compared to our initial model, the simulation results agree well with experimentally-measured trajectory data with slip. Initially we thought that only high robot velocity and acceleration governed the resulting slipping motion. However, we learned that the solid material existing in the discontinuities between omni-directional wheel rollers plays an equally important role in determining omni-directional mobile robot dynamic slip motion, even at low rates and accelerations.

1. INTRODUCTION

Research interest in mobile robots has been tremendous in the past few years, as evidenced by review articles (e.g. [1], [2]).

Some researchers have considered slipping motion between the wheels and motion surface in mobile robots and vehicles. Choi and Sreenivasan have designed articulated wheeled vehicles with variable-length axles to eliminate kinematic wheel-surface slipping [3]. Hamdy and Badreddin developed a tenth-order nonlinear dynamic model for a wheeled mobile robot that includes slip between the driven wheels and the ground [4]. Rajagopalan developed an expression for the angular velocity of wheel slip for wheeled mobile robots with different combinations of steering and driving wheels, considering kinematics only [5]. Shekhar derives a dynamic model for mobile robots with wheel slip using accessibility and controllability in nonlinear control theory [6]. Balakrishna and Ghosal present a traction model accounting for slip in nonholonomic wheeled mobile robots [7]. Scheding et al. present experimental evaluation of a navigation system that handles autonomous vehicle wheel slip via sensor feedback [8].

Several research groups are developing omni-directional mobile robots and vehicles due to inherent agility benefits. Jung et al. developed an omni-directional mobile robot base for the RoboCup competition [9]. RoboCup (www.robocup.org) is an international competition wherein teams of autonomous mobile robots compete in the game of soccer. Moore et al. present a control algorithm for an omni-directional six-wheeled vehicle; each wheel is steered and driven independently [10]. Watanabe et al. present a controller for an omni-directional mobile robot for service applications [11]. Witus investigates a 6-wheeled omni-directional vehicle with tire inflation control [12].

A recent article presented a clever design plus experimental results for a spherical rolling robot [13]; however, this mobile robot is not omni-directional and a no-slip condition was assumed. Our literature search revealed only two papers which mentioned slip in omni-directional wheeled robots. Mori et al. claim that their vehicle avoids tire slippage by design since their omni-directional motion base decouples steering and driving [14]. Dickerson and Lapin present a controller for omni-directional Mecanum-wheeled vehicles, with wheel slip detection and compensation [15].

The current paper presents a dynamic model for omni-directional mobile robots that includes slipping between the wheels and the motion surface. This paper was motivated by a need in the Ohio University cross-disciplinary RoboCup team: in preliminary hardware testing of our omni-directional three-wheeled player robot, significant slipping occurred which necessitated development of a dynamic model with slip. Though our work is motivated by RoboCup, the result is a general dynamic model for omni-directional wheeled vehicles including slip. Our model includes both friction in the wheel rolling direction and in the transverse direction (normal to the first). One important issue turned out to be differing frictional characteristics due to the discontinuities between rollers in the omni-directional wheels.

This paper first presents our omni-directional robot design, followed by dynamic modeling including slip, a method to experimentally determine the coefficients of friction, and then simulation and experimental results to demonstrate omni-directional mobile robot dynamics considering slip.

Copyright © 2002 by ASME

2. OMNI-DIRECTIONAL ROBOT MODEL

In early evaluation of our three-wheeled omni-directional RoboCup player robot, slipping was encountered between the wheels and the carpet playing field when the robot was in motion. This unexpected behavior motivated the development of a dynamic model including slip. This model is presented in the next section; the current section describes the omni-directional robot hardware and model.

Figure 1 shows the CAD model for the three-wheeled omni-directional RoboCup player and Fig. 2 shows a photograph of the prototype hardware.

Figure 3 shows the top view of our general three-wheeled omni-directional mobile robot model. The variables, used in the dynamic model of the next section, are explained below.

The inertially-fixed frame is $\{0\}$ and the moving Cartesian reference frame is $\{M\}$. The rear wheel is aligned in the X_M direction; the front two wheels are symmetrically-placed, aligned by constant angle δ from the Y_M axis (shown only for the left wheel in Fig. 3). We assume the center of mass for the robot is located at the center of the robot circle, which is the origin of $\{M\}$. This was one of our guiding principles in design. The robot mass is m and the robot mass moment of inertia about the Z_M axis through the center of mass is I. Each wheel center position is given by position vector $\mathbf{r}_i$, from the origin of $\{M\}$ to the center of the wheel. The unit vector $\hat{\mathbf{r}}_i$ in this direction is also the direction of each wheel's angular velocity vector (i.e. $\hat{\mathbf{r}}_i$ is the axle direction). The unit vector $\hat{\mathbf{s}}_i$ is normal to $\hat{\mathbf{r}}_i$, giving the instantaneous direction of each wheel. The Cartesian variables for omni-directional motion are $\mathbf{X} = \{x \quad y \quad \phi\}^T$.

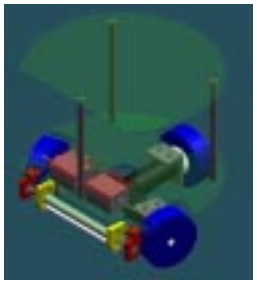

Figure 1. CAD Model

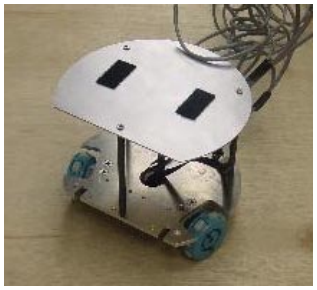

Figure 2. Hardware Photo

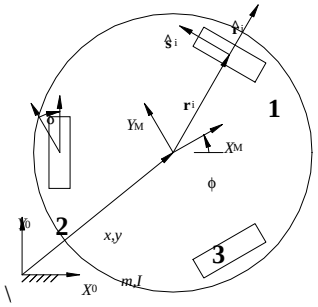

Figure 3. Omni-Directional Robot Model, Top View

The omni-directional motion is enabled via special wheels. Figure 4 shows a commercial omni-directional wheel (kornylak.com) used in our RoboCup mobile robot designs. It is important to note that these wheels were not intended for omni-directional mobile robots; rather, they were developed for material handling applications. For a good discussion on omni-directional wheels for mobile robots, see [16]. Our application dictated economical, commercially-available wheels, which led to our choice of wheel.

As seen in Fig. 4, the axle is mounted normal to the wheel's circle as in a standard wheel. However, the contact with the ground is via rollers that are free to spin about an axis in-line with the circle circumference, normal to the wheel axle. This enables omni-directional motion.

3. OMNI-DIRECTIONAL ROBOT DYNAMICS MODELING

This section presents omni-directional mobile robot modeling with slip included between the wheels and motion surface. The first subsection presents the model, plus the friction model and experimental measurement of the friction coefficients; the second subsection presents a method to experimentally validate our theoretical friction model and measured friction coefficients.

The dynamics model is developed in this subsection for a three-wheeled omni-directional robot, but it applies to any omni-directional robot with three or more wheels. The dynamic model is shown in the top view of Fig. 3 above, and is described in Section 2. Figure 5 shows modeling details for the i^{th} wheel.

Figure 4. Commercial Wheel

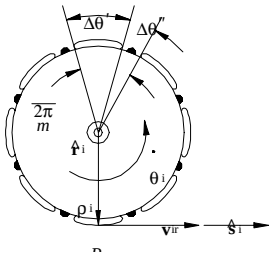

Figure 5. Wheel Detail

As seen in Fig. 5, we denote P_i (i=1,2,3) as the contact point between the i^{th} wheel and the ground. Instantaneously, P_i belongs to the ground and the wheel, but we consider that P_i is on the wheel. The velocity vector $\mathbf{v}_i$ for point P_i is:

$$\mathbf{v}_i = \mathbf{v}_G + \boldsymbol{\omega} \times \mathbf{r}_i + \mathbf{v}_{ir} \tag{1}$$

$\mathbf{v}_G$ is the vehicle center of mass translational velocity, $\boldsymbol{\omega}$ is the vehicle rotational velocity (both translational and rotational velocity vectors are expressed with respect to the inertially-fixed frame $\{0\}$), $\mathbf{r}_i$ is the position vector giving the wheel center position with respect to the moving frame $\{M\}$, expressed in the inertial frame, and $\mathbf{v}_{ir}$ is the peripheral wheel speed with respect to the local frame, expressed in the inertial frame. Note that when $\mathbf{v}_i$ is null, there is no slipping motion.

We can express $\mathbf{v}_{ir}$ as a function of the wheel angular velocity vector $\dot{\boldsymbol{\theta}}_i$ and the wheel radius vector $\boldsymbol{\rho}_i$:

Copyright © 2002 by ASME

$$\mathbf{v}_{ir} = \dot{\boldsymbol{\theta}}_i \times \boldsymbol{\rho}_i \tag{2}$$

The wheel angular velocity vector $\dot{\boldsymbol{\theta}}_i = \dot{\theta}_i \hat{\mathbf{r}}_i$ is the scalar wheel speed $\dot{\theta}_i$ in the unit $\hat{\mathbf{r}}_i$ direction, and the wheel radius position vector $\boldsymbol{\rho}_i$ is scalar wheel radius ρ_i from the wheel center to point P_i. Note the result of (2) is scalar $\rho_i \dot{\theta}_i$ in the unit wheel direction $\hat{\mathbf{s}}_i$ (normal to $\hat{\mathbf{r}}_i$). The next two subsections present our initial and then improved (based on experimental behavior) friction models.

1) Initial Friction Model

There are two directions of wheel/ground friction to consider: the first is friction in the direction of the wheel rotation, $\hat{\mathbf{s}}_i$, and the second is transverse to this direction, $\hat{\mathbf{r}}_i$. Initially our model only included the former case, but initial trials with the omni-directional motion base hardware indicated that we must also include the latter friction case.

For use with friction in the direction of the wheel rotation, the sliding velocity component v_{Wi} in the i^{th} wheel is obtained by dotting the total point P_i velocity from (1) into the $\hat{\mathbf{s}}_i$ unit direction:

$$v_{Wi} = \mathbf{v}_i \bullet \hat{\mathbf{s}}_i = \mathbf{v}_G \bullet \hat{\mathbf{s}}_i + (\omega \times \mathbf{r}_i) \bullet \hat{\mathbf{s}}_i + \rho_i \dot{\theta}_i \tag{3}$$

To convert wheel positions and unit directions described in the local frame (${}^M\mathbf{r}_i$ and ${}^M\hat{\mathbf{s}}_i$) to the inertial frame ($\mathbf{r}_i$ and $\hat{\mathbf{s}}_i$):

$$\hat{\mathbf{s}}_i = {}^0_M\mathbf{R}\,{}^M\hat{\mathbf{s}}_i \qquad \mathbf{r}_i = {}^0_M\mathbf{R}\,{}^M\mathbf{r}_i \tag{4}$$

where:
$${}^0_M\mathbf{R} = \begin{bmatrix} \cos\phi & -\sin\phi \\ \sin\phi & \cos\phi \end{bmatrix} \tag{5}$$

Therefore, (3) becomes:

$$v_{Wi} = \mathbf{v}_G \bullet {}^0_M\mathbf{R}\,{}^M\hat{\mathbf{s}}_i + \left(\omega \times {}^0_M\mathbf{R}\,{}^M\mathbf{r}_i\right) \bullet {}^0_M\mathbf{R}\,{}^M\hat{\mathbf{s}}_i + \rho_i \dot{\theta}_i \tag{6}$$

On the other hand, the transverse sliding velocity component v_{Ti} in the i^{th} wheel, along the wheel axle direction $\hat{\mathbf{r}}_i$ is:

$$v_{Ti} = \mathbf{v}_G \bullet {}^0_M\mathbf{R}\,{}^M\hat{\mathbf{r}}_i + \left(\omega \times {}^0_M\mathbf{R}\,{}^M\mathbf{r}_i\right) \bullet {}^0_M\mathbf{R}\,{}^M\hat{\mathbf{r}}_i \tag{7}$$

If we assume the vehicle weight is equally distributed on each wheel, the friction force exerted on wheel *i* by the motion surface through point P_i is given by:

$$\mathbf{F}_i = -\frac{mg}{3}\left(\mu_W(v_{Wi})\,{}^0_M\mathbf{R}\,{}^M\hat{\mathbf{s}}_i + \mu_T(v_{Ti})\,{}^0_M\mathbf{R}\,{}^M\hat{\mathbf{r}}_i\right) \tag{8}$$

where $\mu_W(\cdot)$ is a function representing the friction coefficient versus the sliding velocity in the direction of the wheel rotation and $\mu_T(\cdot)$ is the friction coefficient for the transverse wheel direction.

The dynamic equations are:

$$m\ddot{x} = \sum_{i=1}^{3} \hat{\mathbf{x}} \bullet \mathbf{F}_i \qquad m\ddot{y} = \sum_{i=1}^{3} \hat{\mathbf{y}} \bullet \mathbf{F}_i \qquad I\ddot{\phi} = \sum_{i=1}^{3} \hat{\mathbf{z}} \bullet (\mathbf{r}_i \times \mathbf{F}_i) \tag{9}$$

where $\hat{\mathbf{x}}, \hat{\mathbf{y}}, \hat{\mathbf{z}}$ are the unit direction vectors of the inertial frame. The nonlinear dynamic equations are of the form $\ddot{\mathbf{X}} = \mathbf{f}(\mathbf{X}, \dot{\mathbf{X}})$:

$$\begin{Bmatrix} \ddot{x} \\ \ddot{y} \\ \ddot{\phi} \end{Bmatrix} = \begin{Bmatrix} -\frac{g}{3}\sum_{i=1}^{3} \hat{\mathbf{x}} \bullet \left(\mu_W(v_{Wi})\,{}^0_M\mathbf{R}\,{}^M\hat{\mathbf{s}}_i + \mu_T(v_{Ti})\,{}^0_M\mathbf{R}\,{}^M\hat{\mathbf{r}}_i\right) \\ -\frac{g}{3}\sum_{i=1}^{3} \hat{\mathbf{y}} \bullet \left(\mu_W(v_{Wi})\,{}^0_M\mathbf{R}\,{}^M\hat{\mathbf{s}}_i + \mu_T(v_{Ti})\,{}^0_M\mathbf{R}\,{}^M\hat{\mathbf{r}}_i\right) \\ -\frac{mg}{3I}\sum_{i=1}^{3} \hat{\mathbf{z}} \bullet \left[{}^0_M\mathbf{R}\,{}^M\mathbf{r}_i \times \left(\mu_W(v_{Wi})\,{}^0_M\mathbf{R}\,{}^M\hat{\mathbf{s}}_i + \mu_T(v_{Ti})\,{}^0_M\mathbf{R}\,{}^M\hat{\mathbf{r}}_i\right)\right] \end{Bmatrix} \tag{10}$$

In our simulation we use the following simplified formulas for coefficient of friction:

$$\mu_W(v_W) = \mu_{W\max}\frac{2}{\pi}\operatorname{atan}(k v_W)$$
$$\mu_T(v_T) = \mu_{T\max}\frac{2}{\pi}\operatorname{atan}(k v_T) \tag{11}$$

where $\mu_{W\max}$, $\mu_{T\max}$, and *k* are constants, and v_W and v_T are the sliding velocity magnitudes in the wheel rotation and transverse directions, respectively.

Notice that in our friction model, the dynamic friction coefficient is assumed to be constant and equal to the constant static friction coefficient; we assume that this simplified model will be sufficient to match experimental results. Equations (11) are artificial functions to conveniently represent the friction coefficients stably in simulation, avoiding algorithmic problems that may arise when using a discontinuous function at zero sliding velocity. This is a common approach; for example see [17] which presents a parametric model and experimental results for tire-road friction coefficients for automotive applications with different road conditions. The *k* constant governs the steepness of the change between positive and negative $\mu_{W\max}$ and $\mu_{T\max}$ about zero sliding velocity. Note that (11) defines positive friction coefficient to correspond with positive sliding velocity; the opposite sign behavior (Coulomb friction acts opposite to the sliding direction) is taken into account in (8). Also, $\mu_{T\max}$ is much less than $\mu_{W\max}$ due to the design of the omni-directional wheels used, with smaller friction in the transverse direction than the primary driving direction, owing to the passive rolling cylinders (see Fig. 4).

2) Improved Friction Model

We noticed that, for our choice of wheel, the friction coefficient is a function of the wheel angle θ_i. When the rigid wheel material between two rollers is in contact with the motion surface (see Fig. 5), the friction coefficients change. This undesirable behavior cannot be blamed on the wheel manufacturer since the wheels were not made for use in omni-directional mobile robots. We account for this phenomenon by introducing nonlinear friction coefficients as a function of the sliding speeds ***and*** wheel angle. Let *m* be the number of rollers in the wheel (*m*=8 in Figs. 4 and 5). Each roller and fixed portion is within angular sector $2\pi/m$. Each sector can be split into two different (roller and fixed) portions with different friction coefficients: $\Delta\theta' + \Delta\theta'' = 2\pi/m$ as seen in Fig. 5. Therefore, we have different friction coefficients according to which part of the sector is in contact with the motion surface at a given time. In our hardware wheel, $\Delta\theta'$ accounts for 90% of each angular sector $2\pi/m$ and $\Delta\theta''$ accounts for 10%.

Copyright © 2002 by ASME

To summarize, our improved friction model is the same as (11), but we use roller values for friction coefficient ($\mu'_{W\max}$ and $\mu'_{T\max}$) when the wheel angle is within the $\Delta\theta'$ sector and we use rigid material values ($\mu''_{W\max}$ and $\mu''_{T\max}$) when the wheel angle is within $\Delta\theta''$.

3) Experimental Friction Coefficient Measurement

We measured experimental values for $\mu'_{W\max}$, $\mu'_{T\max}$, $\mu''_{W\max}$, and $\mu''_{T\max}$ for use in the dynamic simulation, for two motion surfaces: paper and carpet. In order to estimate $\mu'_{W\max}$, we built a special vehicle in which all the wheels were aligned along a common direction. Each wheel angle was fixed in such a way that only the rollers were in contact with the motion surface. The surface was made up of a rigid board covered with paper or carpet. The square board was pivoted on one edge. The vehicle was placed so that all wheel axes were parallel to the pivoting edge. Then we gradually lifted the board until the special vehicle slid. $\mu'_{W\max}$ was determined as the tangent of the angle between the lifted board and the horizontal plane. To measure $\mu'_{T\max}$, we repeated the above procedure, placing the special vehicle so that all wheel axes were perpendicular to the pivoting edge. Again in this case only the rollers were in contact with the motion surface. $\mu''_{W\max}$ and $\mu''_{T\max}$ were measured in the same way, but in these cases the wheel angle was fixed so that only the wheel sector between two consecutive rollers was in contact with the motion surface. The results are shown in Table I below.

Table I. Experimental Friction Coefficients

Surface	$\mu'_{W\max}$	$\mu'_{T\max}$	$\mu''_{W\max}$	$\mu''_{T\max}$
Paper	0.26	0.09	0.47	0.47
Carpet	0.25	0.15	0.56	0.56

The results of Table I were averaged over several trials. For each surface, the transverse roller friction ($\mu'_{T\max}$) is much smaller than that in the wheel rotation direction ($\mu'_{W\max}$). The wheel rotation direction friction coefficients are nearly the same for paper and carpet; for the material between the rollers, the carpet value is higher than that of the paper surface. As expected, the wheel and transverse coefficients of friction ($\mu''_{W\max}$ and $\mu''_{T\max}$) are identical for the material between the rollers.

4. SIMULATED AND EXPERIMENTAL RESULTS

This section presents simulated and experimental results to demonstrate omni-directional mobile robot motion considering slip. Initially, we thought that high accelerations and velocities would be the determining factor in producing slipping motion. Experimental work revealed that a more significant factor in slip with our robot was the solid wheel material in-between the wheel roller discontinuities (see Fig. 5). These solid portions made contact with the motion surface in-between the desired roller contact. As presented in Section 3.2, this led to the development of an improved friction coefficient model, dependent on normal and transverse sliding velocity *and* the wheel angle. This section has three subsections: first, the simulation results are presented, using the simpler friction coefficient model; next, the experimental procedure and results are presented; last, the improved friction coefficient model simulation results are presented and compared with the experimental results.

In all three subsections, the same motion condition is used: we command straight-line motion from initial point $\mathbf{X}_0 = \{0.0 \quad 0.0 \quad 0\}^T$ to final point $\mathbf{X}_F = \{0.4 \quad 0.0 \quad 0\}^T$ (*m*) in a specified time of $t_F = 3.5$ *sec*. We consider only *X* motion since, due to robot symmetry, *Y* motion is inherently less affected by slip. Figure 3 shows our robot hardware geometry (our design has $\delta = 15^\circ$: we were driven to this choice by RoboCup size constraints; $\delta = 30^\circ$ is preferable for robot symmetry). The motion is commanded in the inertial frame, $\{0\}$ in Fig. 3. Robot orientation ϕ is also important in slip dynamics, but the pure *X* motion will also demonstrate (unwanted) orientation slip motion. Robot orientation is commanded as zero for the motion example.

Since we wish to demonstrate slipping, we make no attempt to smooth the commanded velocity motion from rest or ending at rest. Hence, the simulated commanded wheel acceleration is infinite at the start and the deceleration is infinite at the end of the time period. Of course, neither the real or simulated robot can achieve infinite acceleration or deceleration, but the high accelerations at the start and end are sufficient to cause slip. Constant velocity is commanded in between the start and end. Clearly for omni-directional mobile robot applications we need smoother trajectory generation, perhaps using 5th-order polynomials for wheel displacements.

For this motion example, using inverse rate kinematics, the required constant wheel angular speeds are $\dot{\theta}_1 = \dot{\theta}_2 = +1.16$ and $\dot{\theta}_3 = -4.50$ (*rad*/*s*); note the wheel numbering convention is given in Fig. 3. With this motion example, we consider two motion surfaces to include different levels of friction: a smooth paper surface and a rough carpet surface. The coefficients of friction for use in the initial and improved simulations were presented in Section 3.1.3, measured experimentally.

A. Initial Simulation Results

We developed a Matlab Simulink model to simulate omni-directional mobile robot dynamic motion considering slip. In this subsection we present simulated dynamics results using the initial friction model of Section 3.1.1. The simulated motion condition, surfaces, and friction coefficients are described above. To save space, we only show the simulated case with the paper motion surface.

Figure 6a shows the Cartesian displacements and Fig. 6b shows the associated sliding speeds in the wheel directions for each wheel, for the simulated motion. In Fig. 6b, the simulated sliding speeds for wheels one and two are identical due to symmetry. As seen in Fig. 6b, slipping is encountered at the

Copyright © 2002 by ASME

start and end of motion (due to the infinite commanded acceleration and deceleration), but not in the middle. The effect, seen in Fig. 6a, is that *x* falls short by 14 *mm* its goal of 0.4 *m*, while *y* drifts -9 *mm* from the desired zero. ϕ drifts from its commanded value of zero by -0.016 *rad* at the end; in the middle of motion, the ϕ drift is larger. From approximately $t = 0.25$ *sec* to $t = t_F = 3.5$ *sec*, the *x* motion is linear, which means constant velocity has been achieved and the simulation predicts no unwanted slipping in this range.

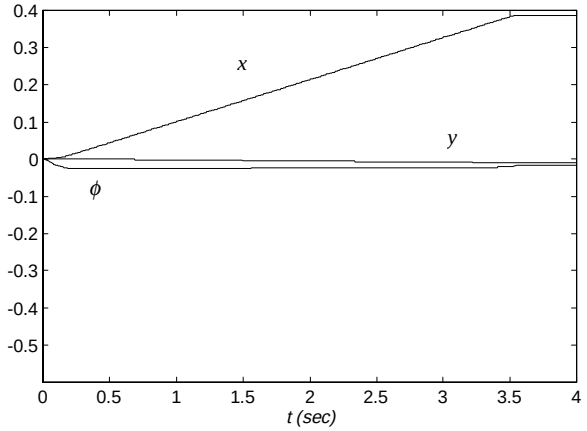

Figure 6a. Cartesian Displacements

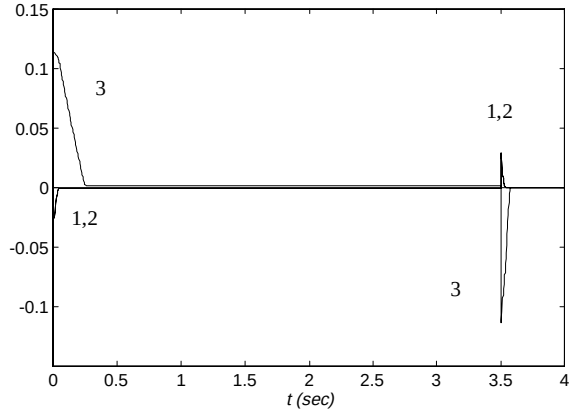

Figure 6b. Wheel Sliding Speeds (m/s)

B. Experimental Procedure and Results

Experiments were performed to validate the results of our simulation work, using both paper and carpet motion surfaces. Our mobile robot was tethered for the experiments; eventually our mobile robots will be free, the on-board PCs communicating with the host PC via wireless Ethernet. To control the robot during the experimental trials, WinCon 3.1 in conjunction with Simulink was used. This enabled us to use a Quanser Multi-Q3 board to control the motor angular velocities through a feedback loop. The experimental robot was shown earlier in Fig. 2. Please note that the robot cables must be held manually to avoid constraining the robot motion. Experimental trajectories were traced by attaching a lightweight pencil to the robot center of mass, for the paper surface. This was not feasible for the carpet surface, so only the end points and final orientations were recorded in the carpet cases.

Another way to present the earlier simulation result from Figs. 6 is given in Fig. 7, plotting *y* vs. *x*. The experimental data is included for comparison.

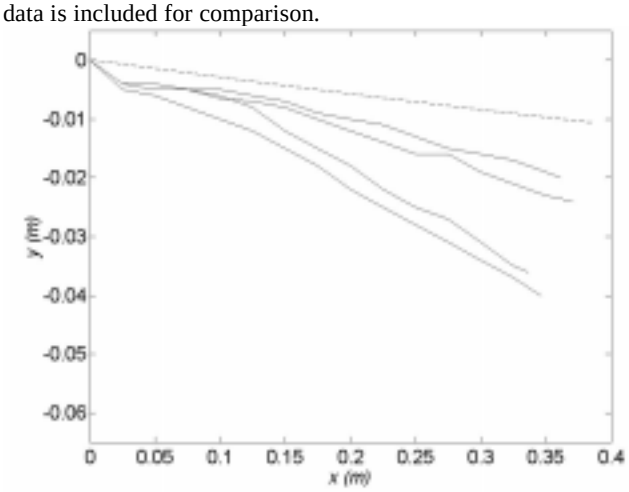

Figure 7a. Simulated (dashed) and Experimental (solid) Results for Paper Motion Surface

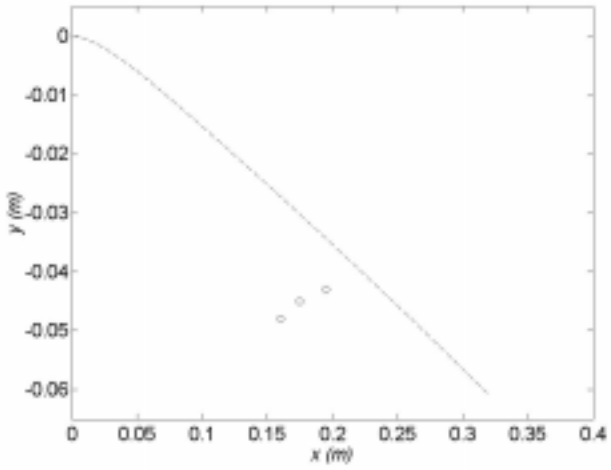

*Figure 7b. Simulated (dashed) and Experimental (*O*) Results for Carpet Motion Surface*

In Fig. 7a, the dashed curve is the simulated result using the initial friction coefficient model and the paper motion surface; this curve was obtained simply by plotting *y* vs. *x* (rather than vs. time *t*) from Fig. 6a. The four solid curves are the results of the four experimental trials for the same motion case, with the paper motion surface. In Fig. 7b, the three single **O** points are the ending points for the three experimental trials with the carpet motion surface (these cases also tried to obtain pure *X* motion from 0 to 0.4 *m*; no trajectory is available as explained above). The dashed curve in Fig. 7b is the simulated result using the initial friction coefficient model and the carpet motion surface (not previously shown).

Clearly from Figs. 7, the simulated results do not agree well with the experimental results, when using the initial friction model and either motion surface, paper or carpet. This poor result motivated the need for an improved friction

Copyright © 2002 by ASME

coefficient model; this was presented in Section 3.1.2 and is now simulated in the following subsection.

C. Improved Simulation Results

In an attempt to improve the poor simulation/experimental agreement of Fig. 7, the improved friction coefficient model of Section 3.1.2 is implemented in simulation in this subsection, and then compared with the existing experimental data. The improved friction model accounts for the rigid material in the discontinuities between wheel rollers (see Fig. 5).

Figures 8 show simulated results for the exact same motion input case as for Figs. 6; Figs. 8 include the real-world effect of material between the wheel rollers. Figure 8a shows the Cartesian displacements and Fig. 8b shows the associated sliding speeds v_{Wi} for each wheel, for the simulated pure X motion on the paper surface. Again in Fig. 8b, the simulated sliding speeds for wheels one and two are identical due to symmetry. As seen in Fig. 8b, slipping again is encountered at the start and end of motion. In addition, wheel three experiences significant slip during the middle of the motion; this was not predicted by the initial model. The effect, seen in Fig. 8a, is that x falls short by 53 *mm* its goal of 0.4 *m*, while y drifts -22 *mm* from the desired zero. ϕ drifts from its commanded value of zero by -0.111 *rad* in the worst case at the end. All three Cartesian drifts are much larger than predicted in Fig. 6a.

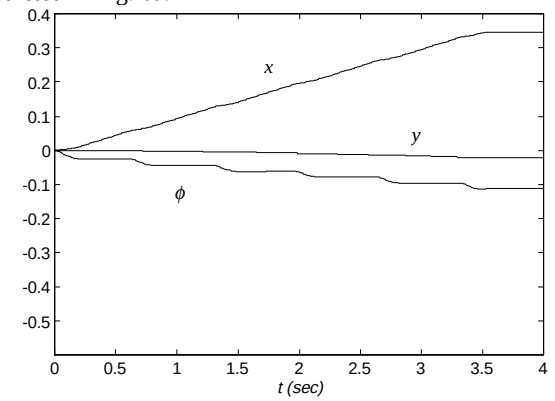

Figure 8a. Cartesian Displacements

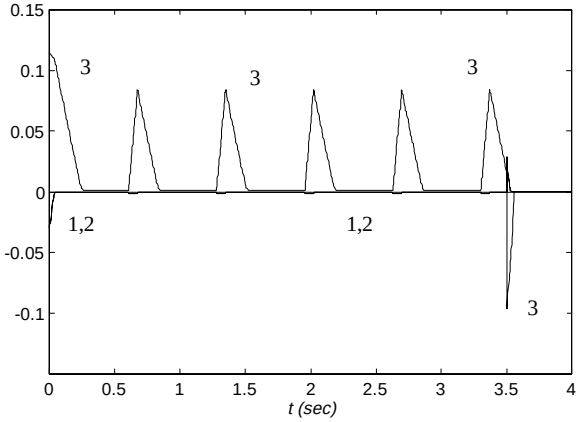

Figure 8b. Wheel Sliding Speeds (m/s)

Figure 9 compares the experimental data with this new, improved simulation, plotting y vs. x. The experimental data of Fig. 9 is identical to that of Fig. 7.

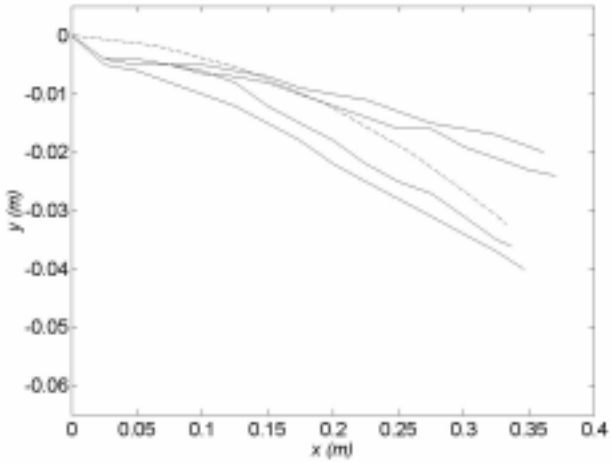

Figure 9a. Improved Simulated (dashed) and Experimental (solid) Results for Paper Motion Surface

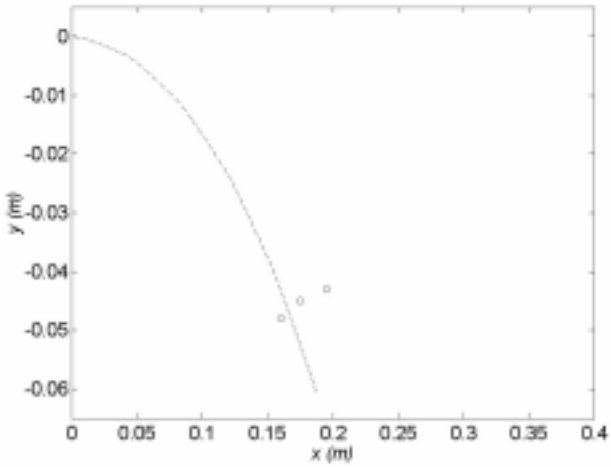

*Figure 9b. Improved Simulated (dashed) and Experimental (*O*) Results for Carpet Motion Surface*

In Fig. 9a, the dashed curve is the simulated result using the improved friction coefficient model and the paper motion surface; this curve was obtained simply by plotting y vs. x (rather than vs. time t) from Fig. 8a. The four solid curves are the experimental results for the same motion case, with the paper motion surface. Clearly, the agreement is much better than that displayed in Fig. 7a with the initial friction model. The three single **O** points in Fig. 9b are the same experimental ending points with the carpet motion surface as shown in Fig. 7b. The dashed curve in Fig. 9b is the simulated result using the improved friction coefficient model and the carpet motion surface (not previously shown); this curve agrees much better with the experimental data endpoints for the carpet surface, compared to Fig. 7b.

Figures 7 and 9 ignore the mobile robot orientation ϕ. For the paper motion surface, the simulated (improved friction model) ending value of ϕ is -0.111 *rad*. No experimental data

Copyright © 2002 by ASME

is available for this case, since the four experimental trials all ended with very small ϕ, close to the angular measurement precision. Even so, the agreement is good qualitatively since the simulated ending angle is also small. For the carpet motion surface, the simulated ending value of ϕ is 0.558 *rad*, which compares favorably with the measured experimental values of 0.524, 0.506, and 0.489 rad (left-to-right for the experimental **O**s of Fig. 9b).

As mentioned earlier, we assumed the dynamic friction coefficient is equal to the static friction coefficient. Perhaps better simulation/experimental agreement would be obtained by use of a combined friction coefficient model where the dynamic friction is less. This is difficult to measure, and we are satisfied with the agreement shown in Fig. 9, using static coefficients of friction only.

5. CONCLUSION

This paper presents a dynamic model for omni-directional wheeled mobile robots and vehicles, considering slipping between the wheels and motion surface. We derived the dynamics model and experimentally measured the friction coefficients; we also validated our friction model by experimentally measuring the maximum force causing slip at various robot orientations (not included to save space). Simulation examples were then presented to demonstrate slipping motion; the initial friction model results did not agree with experimental trajectory data. Therefore, an improved friction model was developed, considering the solid material in the discontinuities between omni-directional wheel rollers. With this improved friction model the simulation agreed well with the experimental data. Two motion surfaces were used in simulation and experiments, with different friction properties: paper and carpet.

During our initial modeling and experimental work, we thought that omni-directional robot slip dynamics would be limited by high velocities and accelerations. This is still true; however, we learned that, for our robot design, an equally significant factor in slip dynamics is the solid material between rollers, even at low motion rates and accelerations. Our RoboCup team response was to file away as much of that material as possible to avoid contact in these sectors. However, this article is pertinent to any omni-directional mobile robot design with or without discontinuity between rollers. Our work demonstrated reasonable simulation/experimental agreement and we feel that we have captured the slip dynamics behavior of our design. A future improvement is to use static and dynamic coefficients of friction; due to our demonstrated agreement, we conclude that the static coefficients of friction are adequate. For different omni-directional robot designs, our modeling and simulation work will apply, but significant experimental work is still required to measure the various friction coefficients and to fully understand the dynamic slip behavior.

REFERENCES

[1] C.C. De Wit, "Trends in Mobile Robot and Vehicle Control", *Control Problems in Robotics and Automation*, 151-175, 1998.

[2] J. Borenstein, H.R. Everett, and L. Feng, "Mobile Robot Positioning: Sensors and Techniques", *Journal of Robotic Systems*, 14: 231-249, 1997.

[3] B.J. Choi and S.V. Sreenivasan, "Gross Motion Characteristics of Articulated Mobile Robots with Pure Rolling Capability on Smooth Uneven Surfaces", *IEEE Transactions on Robotics and Automation*, 15(2): 340-343, 1999.

[4] A. Hamdy and E. Badreddin, "Dynamic Modeling of a Wheeled Mobile Robot for Identification, Navigation and Control", *IMACS Conference on Modeling and Control of Technological Systems*, 119-128, 1992.

[5] R. Rajagopalan, "A Generic Kinematic Formulation for Wheeled Mobile Robots", *Journal of Robotic Systems*, 14: 77-91, 1997.

[6] S. Shekhar, "Wheel Rolling Constraints and Slip in Mobile Robots", *Proceedings of the IEEE International Conference on Robotics and Automation*, 3: 2601-2607, 1997.

[7] R. Balakrishna and A. Ghosal, "Modeling of slip for wheeled mobile robots", *IEEE Transactions on Robotics and Automation*, 11(1):126 –132, 1995.

[8] S. Scheding, G. Dissanayake, E.M. Nebot, and H. Durrant-Whyte, "Experiment in Autonomous Navigation of an Underground Mining Vehicle", *IEEE Transactions on Robotics and Automation*, 15(1): 85 –95, 1999.

[9] M.-J. Jung, H.-S. Kim, S. Kim, and J.-H. Kim, "Omni-Directional Mobile Base OK-II", *Proceedings of the IEEE International Conference on Robotics and Automation*, 4: 3449-3454, 2000.

[10] K.L. Moore, M. Davidson, V. Bahl, S. Rich, and S. Jirgal, "Modeling and Control of a Six-Wheeled Autonomous Robot", *Proceedings of the American Control Conf*, 3: 1483-1490, 2000.

[11] K. Watanabe, Y. Shiraishi, S. Tzafestas, J. Tang, and T. Fukuda, "Feedback Control of an Omni-directional Autonomous Platform for Mobile Service Robots", *Journal of Intelligent and Robotic Systems*,22: 315-330, 1998.

[12] G. Witus, "Mobility Potential of a Robotic 6-Wheeled Omni-Directional Drive Vehicle (ODV) with Z-Axis and Tire Inflation Control", *Proceedings of SPIE*, 4024: 106-114, 2000.

[13] S. Bhattacharya and S. Agrawal, "Spherical Rolling Robot: Design and Motion Planning Studies", *IEEE Transactions on Robotics and Automation*, 16(6): 835-839, 2000.

[14] Y. Mori, E. Nakano, T. Takahashi, and K. Takayama, "Mechanism and Running Modes of New Omni-Directional Vehicle ODV9", *JSME International Journal, Series C*, 42(1): 210-217, 1999.

[15] S.L. Dickerson and B.D. Lapin, "Control of an Omni-Directional Robotic Vehicle with Mecanum Wheels", *National Telesystems Conference* Proceeding, 1: 323-328, 1991.

[16] F.G. Pin and S.M. Killough, "A New Family of Omni-directional and Holonomic Wheeled Platforms for Mobile Robots", *IEEE Transactions on Robotics and Automation*, 10(4): 480-489, 1994.

[17] F. Gustafsson, "Slip-Based Tire-Road Friction Estimation", *Automatica*, 33(6): 1087-99, 1997.

[18] H. Yong-Seob, L. Jihong, and T.C. Hsia, "A Recursive Dimension-Growing Method for Computing Robotic Manipulability Polytope", *Proceedings of the IEEE International Conference on Robotics and Automation*, 2569-74, 2000.

Copyright © 2002 by ASME